Pandit, S., Hornung, B., Dunning, G., Preston, T., Brazener, K., & Orr-Ewing, A. (2017). Primary vs. secondary H-atom abstraction in the Cl-atom reaction with n-pentane. *Physical Chemistry Chemical Physics*, *19*, 1614-1626. https://doi.org/10.1039/C6CP07164C

Primary vs Secondary H-atom Abstraction in the Cl-Atom Reaction with *n*-Pentane

Shubhrangshu Pandit, Balázs Hornung, Greg T. Dunning, Thomas J. Preston,[1] Kristian Brazener and Andrew J. Orr-Ewing*

School of Chemistry, University of Bristol, Cantock's Close, Bristol BS8 1TS, UK.

[1] *Current address: Institute for Energy Technology, Instituttveien, 18, NO-2007 Kjeller, Norway.*

* Author for correspondence

e-mail: a.orr-ewing@bristol.ac.uk

Tel: 0117 9287672

Abstract

Velocity map imaging (VMI) measurements and quasi-classical trajectory (QCT) calculations on a newly developed, global potential energy surface (PES) combine to reveal the detailed mechanisms of reaction of Cl atoms with *n*-pentane. Images of the HCl(v=0, J=1, 2 and 3) products of reaction at a mean collision energy of 33.5 kJ mol^{-1} determine the centre-of-mass frame angular scattering and kinetic energy release distributions. The HCl products form with relative populations of J= 0–5 levels that fit to a rotational temperature of 138 $\pm$ 13 K. Product kinetic energy release distributions agree well with those derived from a previous VMI study of the pentyl radical co-product [Estillore et al., J. Chem. Phys. 2010, **132**, 164313], but the angular distributions show more pronounced forward scattering. The QCT calculations reproduce many of the experimental observations, and allow comparison of the site-specific dynamics of abstraction of primary and secondary H-atoms. They also quantify the relative reactivity towards Cl atoms of the three different H-atom environments in *n*-pentane.

1. Introduction

Reactions of organic molecules with Cl atoms contribute to atmospheric oxidation pathways in the marine boundary layer and coastal regions of the lower troposphere,[1,2] with H-atom abstraction followed by O_2 addition providing a source of peroxy radicals.[3,4] Cl can also add across C=C bonds in unsaturated organic compounds such as isoprene,[5,6] and recent studies examined the subsequent pathways to HCl elimination.[7–10] The Cl-atom reactions with methane, ethane, larger alkanes and other organic compounds serve as model systems for the study of dynamics of gas-phase reactions of polyatomic molecules,[11–13] with detailed investigations performed in a number of laboratories.[14–23] Selected examples have also been the subjects of computer simulation using global potential energy surfaces[10,24] or direct dynamics calculations,[25–27] with calculated product quantum state populations and state-resolved differential cross sections that are in reasonable accord with experimental data. A combination of the experimental and computational outcomes has highlighted the importance of weak interactions in the post-transition state (TS) region in determining product quantum state distributions.[12,25,28–31] Chlorine atom reactions with alkanes, alkenes, alcohols and other organic compounds are also being examined in liquid solutions to explore how solvents modify the reaction rates and dynamics.[32–35]

The reactions of Cl atoms with larger alkanes than ethane reveal a variety of mechanistic complexities,[13] and these are the subject of the current experimental and computational study of the Cl + *n*-pentane reaction. For example, the relative reactivities and scattering dynamics may differ for abstraction of primary and secondary hydrogen atoms, as might the mechanisms of reactions of structural isomers. Tyndall *et al*.[36] addressed the question of relative reactivities and reported 43 ± 3 % 1-propyl and 57 ± 3 % 2-propyl yields in the reaction of Cl with propane at 296 K, which agree within the mutual uncertainties with more recent measurements at 298 K by Choi *et al*.[33] For the Cl + *n*-butane reaction, the respective 1-butyl and 2-butyl radical yields from the study by Tyndall *et al*. were 29 ± 2 % and 71 ± 2 %. Selective deuteration of primary or secondary sites provides some

further evidence for a preference for abstraction from secondary (or tertiary) sites by Cl atoms at super-thermal collision energies,[34,37,38] although the isotopic substitution may itself modify the reactivity. However, Estillore *et al*.[39] studied the Cl atom reaction with $CD_3CH_2CH_2CD_3$ and concluded that the angular scattering distributions for the channels forming HCl and DCl were identical for chosen collision energies in excess of 20 kJ mol^{-1}. Suits and coworkers also explored the dependence of the scattering dynamics on alkane isomer for the examples of *n*-butane *versus* isobutene,[40] and *n*-pentane *versus* isopentane and neopentane,[19] in all cases by detection of the radical products.

The thermal rate coefficient for the Cl + *n*-pentane reaction reported by Seakins and coworkers indicates a fast reaction with little or no activation barrier.[41] This rate coefficient is an average over reaction sites, but the energy released depends on whether a primary or secondary H atom is abstracted:[42]

$$\text{Cl} + n\text{-pentane} \rightarrow \text{HCl} + \text{1-pentyl} \qquad \Delta_r H = -8.4 \text{ kJ mol}^{-1} \qquad \text{(1a)}$$

$$\text{Cl} + n\text{-pentane} \rightarrow \text{HCl} + \text{2-pentyl or 3-pentyl} \qquad \Delta_r H = -22.2 \text{ kJ mol}^{-1} \qquad \text{(1b)}$$

The reactions of Cl with ethane and neopentane, in which only a primary H-atom is available for removal, have reaction enthalpy changes of $\Delta_r H = -8.7 \pm 1.6$ and -10.5 ± 8.4 kJ mol^{-1} respectively that are comparable to reaction (1a).[23,43] The location of primary H atoms at the periphery of an *n*-pentane molecule favours their abstraction in large impact-parameter collisions with Cl atoms, whereas the greater energy release for reaction (1b) instead might promote secondary H-atom abstraction by moving the TS earlier along the reaction coordinate. The current study examines the product energy disposal for signatures of the different thermochemistries of reactions (1a) and (1b) in the reaction dynamics, and analyses angular scattering distributions for evidence of the preferred impact parameters for reaction.

The relationship between the reaction pathway and the quantum states populated in the product HCl remains largely unaddressed for the larger alkane reactions with chlorine, but the extent of HCl

rotational excitation and the associated variation in scattering distributions should be sensitive indicators of the dynamics.[20,23,44] Here, we report rotational level populations for nascent HCl(v=0) products of reaction of Cl atoms with *n*-pentane at an average collision energy of 33.5 kJ mol^{-1}, and velocity map images obtained for HCl(v=0,J=1−3) from which we obtain centre-of-mass (CM) frame angular scattering and translational energy distributions. The outcomes are compared with our recent studies of Cl + ethane [29] and Cl + neopentane reactions,[23] and the complementary studies of Cl + *n*-pentane by Suits and coworkers in which the pentyl radical products were probed.[19] Quasi-classical trajectory (QCT) calculations on a newly constructed potential energy surface (PES) distinguish the different H-atom abstraction channels to form 1-, 2- and 3-pentyl radical products. The global PES was obtained by fitting discrete structure and energy points from *ab initio* electronic structure calculations using the empirical valence bond (EVB) formalism.[45,46] We have previously tested and validated this efficient method for PES generation against experimental data for reactions of Cl atoms with methane and propene.[10,24] The QCT calculations successfully reproduce most of the experimental results, and explore the competition between primary and secondary H atom abstraction pathways.

2. Experimental

The experimental apparatus used for the reported measurements has been described previously,[8,23] and we provide only a brief overview here. Reagent gases (50% Cl_2 in Ar, and ~40% *n*-pentane in Ar, both at backing pressures of 1.5 bar) were introduced into the source region of a linear time-of-flight mass spectrometer (TOF MS) using two separate pulsed valves operating at 10 Hz. The valves pointed parallel to the axis of the TOF MS and were vertically displaced by 17.4 mm, with the upper *n*-pentane / Ar valve aligned along the central cylindrical axis of the instrument. We refer to this arrangement as a "dual-beam" experiment.[21,47] The expansion from the *n*-pentane / Ar valve was partially collimated using a 1-mm diameter skimmer. Photolysis of Cl_2 in the lower gas expansion at a photolysis

wavelength λ_{ph}=355 nm (from the third harmonic of a pulsed Nd:YAG laser) released Cl atoms with mean speed of 1680 m/s, some of which intersected the upper molecular beam and reacted with the *n*-pentane. The resulting collision energies for the Cl + *n*-pentane reaction and comparative studies of the Cl + ethane reaction were 33.5 $\pm$ 8.4 and 27.0 $\pm$ 8.4 kJ mol^{-1} respectively, with the specified ranges mostly arising from the distribution of speeds in the Cl_2 beam and estimated as discussed previously.[23]

HCl reaction products were ionized by 2+1 resonance enhanced multiphoton ionization (REMPI) through the $F^1\Delta$ Rydberg state, with the REMPI wavelength chosen to detect HCl(v=0,J) products in individual rotational levels from J=0 to 5.[48] The probe laser beam exciting the REMPI transition was tuned to wavelengths around 241 nm, and was focused to a spot either within, or just above the *n*-pentane / Ar molecular beam. The consequences of this choice of molecular beam and laser geometries on experimentally determined angular scattering distributions has been discussed in detail elsewhere.[8] Ion optics configured for DC-slice velocity map imaging (VMI) focused the resulting HCl^+ ions onto a detector consisting of a pair of 75-mm diameter microchannel plates and a P47 phosphor screen. A CCD camera captured points of impact of the ions on the detector, which was gated to generate signals for *m*/*z* = 36 ions ($H^{35}Cl^+$) with initial velocity components along the TOF MS axis that were close to zero, giving slices through the 3-dimensional distribution of product recoil velocities. Stepping the time-delay between the photolysis laser and the probe laser pulse from 8.5 to 12.5 μs in intervals of 0.5 μs during velocity map image acquisition minimized any systematic bias towards detection of faster or slower moving reaction products in the laboratory frame arising from forward or backward scatter in the centre-of-mass frame.[21] Conversion of experimental images to kinetic energy distributions used pixel-to-speed conversion factors determined by multi-photon excitation of O_2 at 224.999 nm [49] and Cl atoms from the 355-nm photolysis of Cl_2. The speed resolution of the measurements was ~40 m s^{-1} ($\pm$ 5 pixels in the images).

REMPI spectra of HCl(v=0,J) products were measured by scanning the wavelength of the probe laser at a fixed time delay between the two laser pulses of 10.5 μs (chosen to minimize bias between

detection of HCl products scattered in different directions in the centre-of-mass frame). REMPI signal intensities, integrated across single spectral lines in the R and S branches, were used to deduce relative populations of different J levels. No evidence was found for the formation of HCl(v=1), despite it being energetically accessible under our experimental conditions.

3. Computational details

3.1 Electronic structure calculations

The potential energy surface used in QCT calculations of the dynamics of reaction (1) was constructed from a fit to electronic structure calculations of potential energies at a number of different nuclear geometries. Reactant and product geometries were optimized using unrestricted second-order Møller–Plesset perturbation theory (MP2). Dunning type aug-cc-pVDZ and aug-cc-pV(D+d)Z basis sets were placed on the C and H, and the Cl atoms, respectively.[50–52] The primary and two secondary H-atom elimination channels were explored by carrying out a series of restricted optimizations at selected reactive C–H and H–Cl bond lengths. To avoid convergence problems characteristic of the levels of theory summarized above, the smaller Pople type 6-31(d,p) basis sets were used on all atoms in these calculations.[53,54] The three transition state structures were optimized at the UMP2 / 6-31G (d,p) level. The Gaussian 09 suite of codes was used to perform all these calculations.[55]

The geometries obtained from the MP2 and UMP2 calculations were used in higher level calculations to obtain potential energies. Basis-set superposition error can adversely affect the topography and relative energies of the PES, hence we sought to minimize this error by using an explicitly correlated electronic structure method which approximates the full basis set energies. The energies of all the optimized structures (i.e., reactive scans, reaction and transition state energies) were therefore computed using explicitly correlated, spin-component-scaled, unrestricted second order Møller–Plesset perturbation theory, SCS-MP2-F12, with the aug-cc-pVDZ basis sets of Yousef and Petersen.[56,57]

3.2 Empirical Valence Bond Surface

Our established method of constructing reactive EVB surfaces was applied in this study.[10,24,58] Firstly, the diagonal terms of the EVB matrix were parameterized; these diagonal terms correspond to the reactants, and the six primary and six secondary radical product states. Fits of the rigid SCS-MP2-F12/ aug-cc-pVDZ scans along the internal coordinates of the pentane molecule and pent-1-yl, pent-2-yl and pent-3-yl radicals returned the bond stretching, angle bending, out-of-plane bending and torsion force constants. In addition to these energy terms, intramolecular van der Waals interactions were added to the force fields of the reactant and product molecule. Only the interactions between atoms separated by 4 or 5 bonds were included in the force field, that is the 1,5 and 1,6 van der Waals energy terms. The parameters for these van der Waals interactions were identical to those of the corresponding intermolecular van der Waals terms.

The off–diagonal coupling terms in the EVB matrix describe the reactive regions between the various product and reactant states. The parameters of the van der Waals interactions and of the coupling terms were determined by fitting the SCS-MP2-F12/aug-cc-pVDZ//MP2/6-31G(d,p) scans for primary and two secondary H-atom abstraction channels using a 13×13 EVB matrix, with entries corresponding to reactants and 12 different HCl + pentyl products to incorporate reaction at all H-atom sites. The coupling terms were two-dimensional Gaussian functions which depended on the C–H and H–Cl distances. The four-parameter Buckingham–Corner potential was chosen to account for non-bonding interactions. All of the van der Waals and coupling parameters were adjusted during the EVB fitting; these fits therefore entailed optimization of 34 parameters using 964 *ab initio* electronic structure points in the 0–150 kJ mol^{-1} energy range. The mean unsigned error in the fitted EVB PES was 0.96 kJ mol^{-1}. The functional forms of force field energy terms are specified elsewhere,[10,24] and the list of optimized parameters is provided in the Electronic Supplementary Information. The energetics of the EVB PES are compared to known reaction thermochemistries in Section 4.

3.3 Quasi–Classical Trajectory Calculations

Quasi–classical trajectory calculations were carried out with the Lynx code developed in our group, details of which will be published elsewhere. The vibrational and rotational motions of the pentane were initialised at 100 K (including 417 kJ mol^{-1} of vibrational zero point energy (ZPE) in the pentane), and the relative translational energy of the reactants was 33.5 kJ mol^{-1} to approximate the experimental conditions. The Cl atom was placed at an initial distance of 6 Å from the centre-of-mass of the pentane molecule. This value was determined by running small batches of trajectories at increasing initial separations until the number of reactive events dropped to zero. The impact parameter (from b = 0 – 6 Å) and the orientation of the pentane molecule were sampled randomly using standard methods.[59] A velocity Verlet propagator was employed to integrate trajectories over time, with a step size of 0.1 fs which ensured conservation of energy to better than 0.01 kJ mol^{-1} of the total energy of 460 kJ mol^{-1} (0.002%). In total, 500,000 trajectories were propagated, out of which 81,000 were reactive. Only those trajectories were retained for further investigation in which both of the final products had an internal energy equal to or greater than their respective ZPEs. Consequently, approximately 13,000 trajectories were analysed.

3.4 Analysis of QCT outcomes

The differential cross sections and opacity functions obtained from QCT calculations were expanded in terms of Legendre polynomials.[60,61] The translational energy distribution functions were also approximated by Legendre polynomial expansions of order N_l, as shown in Eq. (2), using a reduced translational energy variable defined by equation (3). Here, $E_{tr,max}$ is the maximum possible translational energy release.

$$P(E_{tr}) = \sum_{l=0}^{N_l} a_l P_l\left(\tilde{E}_{tr}\right) \tag{2}$$

$$\tilde{E}_{tr} = \frac{2E_{tr} - E_{tr,max}}{E_{tr,max}} \tag{3}$$

The QCT calculation outputs can be processed to simulate directly experimental observables such as velocity map images. Full 3D scattering images were synthesized from computational results using a series expansion in terms of real spherical harmonics. Assuming cylindrical symmetry about the initial relative velocity vector, the scattering probability becomes a function of the reduced final relative velocity vector and the scattering angle θ:

$$P(\tilde{v},\theta) = \sum_{n=0}^{N_n}\sum_{l=0}^{N_l} a_{n,l} Y_n^0(\tilde{v},0)\, Y_l^0(\,\theta,0) \qquad (4)$$

Here, the reduced final relative velocity, $\tilde{v}$, is defined in terms of the magnitudes of the final relative velocity ($\underline{u}'$) and the maximum final relative velocity ($\underline{u}'_{max}$) vectors.

$$\tilde{v} = \frac{2\|\underline{u}'\| - \|\underline{u}'_{max}\|}{\|\underline{u}'_{max}\|} \qquad (5)$$

The expansion coefficients are obtained as the expectation values of the coupled real spherical harmonics from a total of N_{sel} trajectories:

$$a_{n,l} = 4\pi\langle Y_n^0(\tilde{v},0) Y_l^0(\,\theta,0)\rangle = \frac{4\pi}{N_{sel}}\sum_{i=1}^{N_{sel}} Y_n^0(\tilde{v}_i,0) Y_l^0(\,\theta_i,0) \qquad (6)$$

4. Results and discussion

Nascent HCl(v=0, J) products from the Cl + *n*-pentane reaction were detected by REMPI and velocity map imaging in specific rotational levels. The analysed results from the VMI studies are presented here in three different sub-sections: HCl rotational level population distributions; quantum-state resolved HCl angular distributions; and total kinetic energy release (TKER) distributions. To explore the competition between the primary and secondary hydrogen abstraction pathways, these experimental results are compared with the outcomes from previous studies of the Cl + ethane[25,27] and Cl +

neopentane reactions.[23] The dynamical differences between the primary and two secondary H-atom abstraction channels are investigated quantitatively with the help of QCT calculations. However, we begin this section with a description of the EVB PES, and a comparison of the computed energy landscape to energies deduced from the thermochemistry of the reactants and products.

4.1 Computed Energetics

Reactions (1a) and (1b) summarize the three possible reaction pathways in the Cl + *n*-pentane reaction. The Cl atom can abstract either a primary H atom from carbons C1 or C5 in the pentane backbone to produce a 1-pentyl radical (denoted here as primary-1), or a secondary H atom from equivalent atoms C2 and C4 (secondary-2) or the central C3 carbon atom (secondary-3), to produce 2-pentyl or 3-pentyl radicals respectively. The *ab-initio* and zero-point-energy corrected energetics of stationary points for the three reaction pathways are compared in Fig.1.

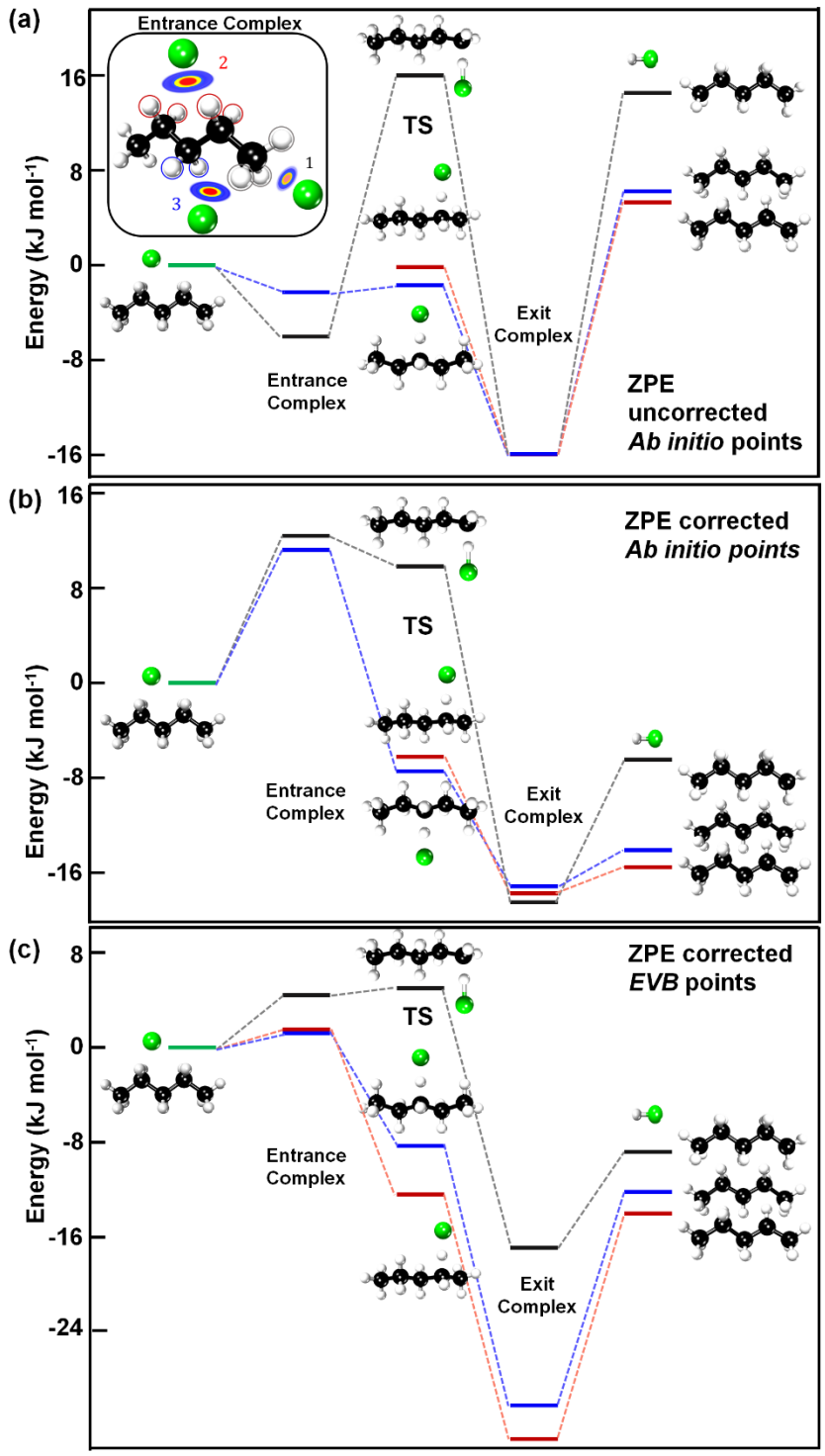

Fig. 1 Energies of key structures for the three competing channels for the Cl + *n*-pentane reaction: primary H abstraction from the C1 or C5 carbon atoms (black lines); secondary H abstraction from C2 or C4 carbon atoms (red lines); secondary H abstraction from the C3 central carbon atom (blue lines). Panel (a) shows the computed *ab-initio* energies of stationary points without zero-point vibrational energy; panel (b) shows the

effects of ZPE correction; and panel (c) shows the energies of the same structures on the EVB PES after correction for zero-point vibrational energies. Three entrance channel complexes are shown in the inserted box. Local minima in the entrance channel of the PES are illustrated schematically as contour maps.

Slices through the *ab initio* PES and the EVB fit are presented in Fig. 2 for the three reaction pathways. Although the thermochemistry predicts both primary and secondary hydrogen abstraction channels of the Cl + *n*-pentane reaction are exothermic, the SCS-MP2-F12/aug-cc-pVDZ reaction energies are endothermic before ZPE correction. Stationary point energies from electronic structure calculations and their global EVB fit are presented in Table 1. After ZPE correction, *ab-initio* reaction energies are -6.5 kJ mol^{-1} and -15.5/-14.1 kJ mol^{-1} for primary and secondary H-atom abstraction channels respectively and the corresponding reaction energies from the EVB fit are -9 kJ mol^{-1} and -14 kJ mol^{-1}. These computed energies are reasonably close to the reaction thermochemistry values. The TSs for secondary channels have submerged barriers (relative to reactants) and the TS for the primary channel is ~13-17 kJ mol^{-1} higher than that for the secondary channels. Pre- and post-reaction complexes are located before and after the TSs. The post-reaction complexes have well depths of ~18 kJ mol^{-1} with respect to reactants for all three reaction channels on the *ab-initio* PES. However, the EVB fit gives a difference of ~ 12 kJ mol^{-1} between 1-pentyl-HCl and 2-pentyl/3-pentyl-HCl post-TS complexes.

Table 1 *Ab-initio* SCS-MP2-F12/aug-cc-pVDZ and EVB energies (in kJ mol^{-1}) of stationary points for the three channels of the Cl + *n*-pentane reaction. Energies are specified relative to an energy of zero for the reactants.

	Method	Energy (kJ mol^{-1})					
		Primary-1		Secondary-2		Secondary-3	
		Uncorrected	ZPE corrected	Uncorrected	ZPE corrected	Uncorrected	ZPE corrected
Products	Ab initio	14.5	-6.5	5.3	-15.5	6.2	-14.1
	EVB	14.5	-8.8	5.3	-14.0	6.2	-12.2
Transition State	Ab initio	16.0	9.8	-0.2	-6.2	-1.7	-7.4
	EVB	14.2	5.0	-4.6	-12.4	-2.8	-8.3
Pre-TS Complex	Ab initio	-6.0	12.4			-2.3	11.0
	EVB	-5.7	4.4	-9.0	1.5	-9.3	1.2
Post-TS Complex	Ab initio	-15.9	-18.5	-16.0	-17.8	-15.9	-17.1
	EVB	-11.1	-16.9	-22.9	-33.0	-24.9	-30.2

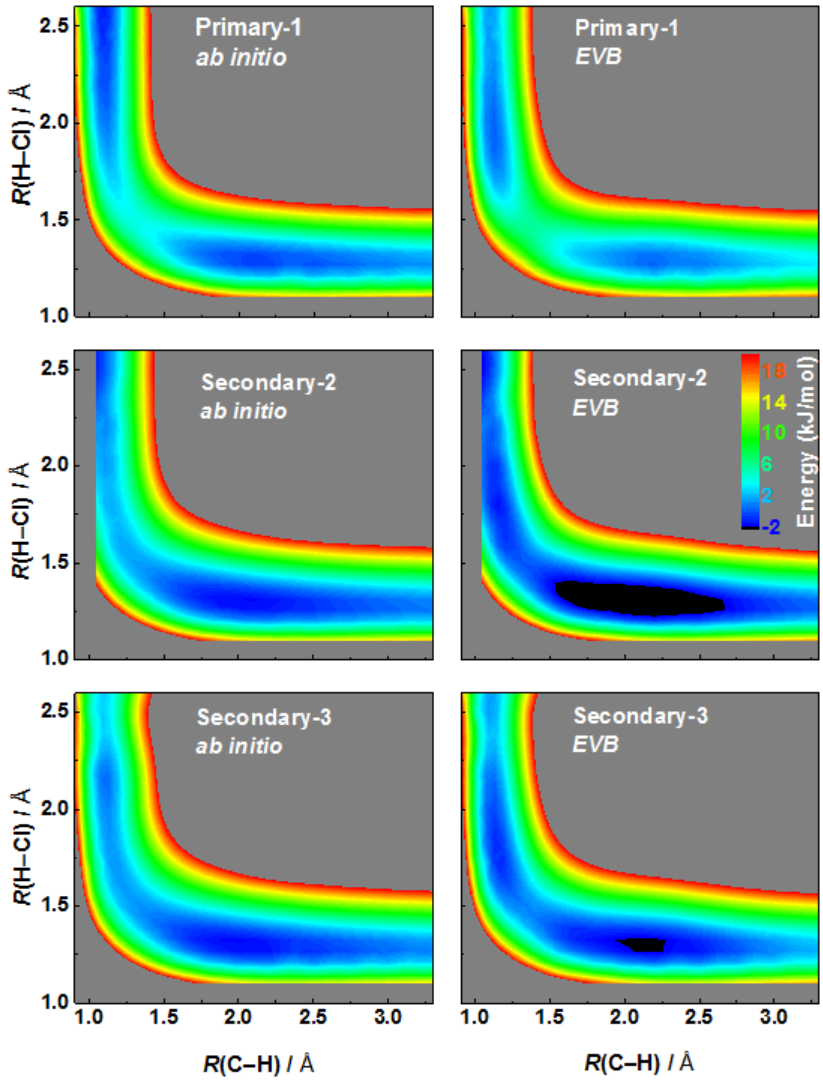

Fig. 2 2D slices of the global PES showing three reaction pathways of the Cl + *n*-pentane reaction. *Ab initio* SCS-UMP2-F12/aug-VDZ // UMP2/6-31G(d,p) and EVB PES scans of the reactive channels are shown in the left and right columns respectively for abstraction from: the C1 or C5 carbon atom (top row); the C2 or C4 carbon atom (middle row); and the C3 carbon atom (bottom row).

The transition state geometry influences the product energy state distributions for different reaction channels, and important geometric parameters of the three different transition states are compared in Table 2. In all cases, the Cl atom aligns almost collinearly with the reactive C-H bond in the transition

state. This collinear geometry affects the HCl rotational distributions, as is discussed in section 4.2. The transition states are neither particularly early nor late along the reaction path: both the C-H and H-Cl distances are longer than their equilibrium distances by ~0.2 Å, although the TS for the more exothermic secondary H abstraction shifts towards the reactants, consistent with Hammond's postulate. Therefore, the reaction exothermicity is expected to partition between product translational and vibrational modes, but the energy released by the reaction is not high enough to excite high frequency H-Cl and C-H stretching modes without converting some of the collision energy into internal motions. Instead, low-frequency modes of the pentyl radical might be excited.

Table 2 Geometric parameters for the three abstraction transition states, deduced from electronic structure calculations. *r* represents a bond length, either in the TS or at equilibrium; *d* denotes a distance from the CM of the pentane molecule to the Cl atom; θ is the $\angle Cl-H-C$ bond angle at the TS.

	r_{C-H}^{eqm} (Å)	r_{C-H}^{TS} (Å)	r_{H-Cl}^{eqm} (Å)	r_{H-Cl}^{TS} (Å)	d_{CM-Cl}^{TS} (Å)	$\theta(\angle Cl-H-C)$ (degree)
Primary-1	1.10	1.36	1.27	1.46	3.78	176.5
Secondary-2	1.10	1.31	1.27	1.49	3.48	175.4
Secondary-3	1.11	1.33	1.27	1.49	2.81	174.6

4.2 HCl rotational distributions

Fig. 3 shows a (2+1) REMPI spectrum of HCl products of reaction (1) under single collision conditions. In this wavelength region, the spectrum is resonance enhanced at the two-photon level by the $F^1\Delta$ Rydberg state. The spectral features are assigned as R- and S-branch lines originating from low J rotational levels, with assignments confirmed by a PGOPHER simulation[62] with spectroscopic constants from Green *et al*.[48] The rotational distributions of HCl (v=0) products from our experimental measurements are shown in Fig. 4(a). Relative populations of HCl (v=0) rotational levels were obtained by correcting the integrated line intensities using factors obtained in a previous study.[29] Nascent HCl products are mostly formed in low rotational levels (J ≤ 5), and the population distribution peaks at J

= 2. These populations are compared in Fig. 4(a) with those determined previously in our laboratory for reactions of Cl atoms with ethane[29] and neopentane[23] and the distributions are similar. The relative populations, when fitted to a Boltzmann distribution, correspond to rotational temperatures of 138 ± 13 K (Cl + *n*-pentane), 123 ± 6 K (Cl + ethane) [29,63] and 82 ± 5 K (Cl + neopentane).[23] The rotational distributions observed in these and other Cl + alkane reactions are generally colder than the predictions of a kinematic model,[64] and are instead indicative of a linear transition state and post-TS dynamics that further suppress rotational excitation of the nascent HCl.[28,30] Our calculations suggest an almost collinear Cl-H-C geometry in the TS and weak post-TS interactions between HCl and the non-polar pentyl radical which are consistent with the experimental outcomes.

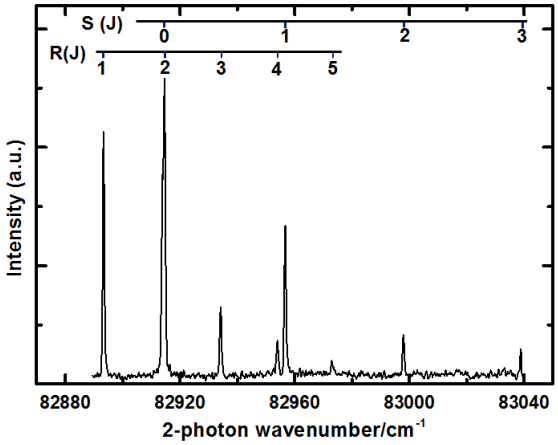

Fig. 3 (2+1) REMPI spectrum of $H^{35}Cl$ ($X^1\Sigma^+$, v′=0) from the Cl + *n*-pentane reaction, resonance enhanced at the two-photon level by the $F^1\Delta$ state. The spectrum shows the low-J regions of the R and S branches as indicated by the combs.

The similarity between the rotational distributions in Fig. 4(a) merits further consideration because the Cl + ethane and Cl + neopentane reactions involve abstraction of a primary H-atom, whereas Cl + *n*-pentane has competing primary and secondary H-abstraction paths. One possible conclusion is that primary H-atom abstraction dynamics dominate the reaction of Cl atoms with *n*-pentane at our super-thermal collision energies. More likely is that both pathways contribute, as suggested by previous studies of ratios of reaction at primary and secondary sites in alkanes,[34,36–39] in which case we deduce

similar dynamics of HCl production at the two abstraction sites despite the difference in $\Delta_r H$ values. The abstraction of a secondary H atom is about twice as exothermic as the primary H-atom channel; if all this additional energy entered HCl rotation, it would result in a ~500 K increase in the rotational temperature. The kinematics of these light-atom transfer reactions approximately conserve the initial collision energy of the reactants into the average kinetic energy of the products.[13,65] For reaction (1), secondary H-atom abstraction might therefore be expected to promote higher internal energy of the two products because of the greater reaction exothermicity. Moreover, the transition state typically moves earlier along the reaction coordinate with increasing reaction exothermicity, which favours internal excitation of products. However, this behaviour is not clearly observed for HCl rotation and vibration following reactions (1a) and (1b).

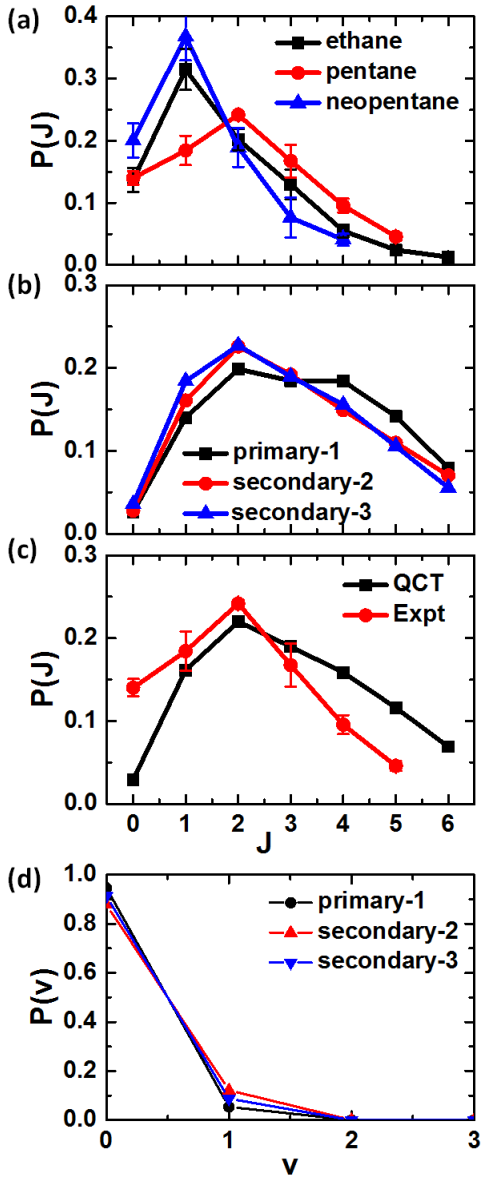

Fig. 4 Comparison of HCl(v=0) rotational level population distributions derived from experimental measurements and QCT calculations. (a) Relative rotational populations of the HCl(v=0) products of reaction of Cl + *n*-pentane (red) obtained from (2+1) REMPI spectra, and comparison with prior measurements from our laboratory for Cl + ethane (black) and Cl + neopentane (blue) reactions at similar collision energies. (b) Computed rotational distributions of HCl (v=0) products from the three pathways for the Cl + *n*-pentane reaction: primary-1 (black), secondary-2 (red), and secondary-3 (blue). (c) Comparison of experimental and QCT-calculated rotational distributions for the Cl + *n*-pentane reaction. The QCT-computed distributions are obtained by summing the outcomes from all reactive trajectories. (d) Computed vibrational level population distributions for the HCl products of the three different reaction channels, using the same colour scheme as in (b). The population distributions are normalized to each sum to unity.

To examine these arguments further, rotational distributions of HCl products from three different abstraction channels were investigated separately in our QCT calculations. Computed rotational level population distributions of HCl (v=0) products are presented in Fig. 4(b). HCl products from all three pathways are rotationally cold ($J \leq 9$). Although the secondary abstraction channel is more exothermic, the HCl rotational distributions are similar for primary and secondary abstraction channels; if anything, the primary channel favours slightly greater HCl rotational excitation. Boltzmann analysis of the populations gives rotational temperatures of 311 ± 15 K for the primary-1 abstraction channel and 286 ± 10 K for both the secondary-2 and secondary-3 abstraction pathways. These rotational temperatures are higher than experimentally observed because of slightly higher simulated population of J = 3 – 6 levels, but both the computed and experimental population distributions peak at J = 2 (Fig. 4(a)). Pathways (1a) and (1b) both have almost collinear Cl-H-C geometries in their transition states, but deviations from the minimum energy pathway through the transition state region, or from linearity in the post-TS region will accelerate rotational motion of the HCl unless weak, post-TS attractive interactions steer the separating HCl and radical back towards collinearity in the C--H–Cl coordinate. On our EVB PES, the post-TS interaction well depths are greater for secondary radical products (see Fig. 2 and Table 1). From the QCT outcomes, and the comparisons between HCl rotational excitation from Cl + *n*-pentane, ethane and neopentane reactions, we conclude that primary vs secondary abstraction cannot be distinguished from experimental measurements of the HCl rotational distributions alone.

4.3 HCl vibrational distributions

Computed vibrational level population distributions for the HCl products of the three different reaction channels are presented in Fig. 4(d). No vibrationally excited HCl ($v \geq 1$) was detected in our experimental measurements, for which the signal-to-noise ratio in the REMPI spectra was 20:1. Therefore, we report the upper limit to be <10% for the formation of vibrationally excited HCl (v=1). The QCT calculations also indicate $\geq$ 90% of HCl products are formed in their vibrational ground state,

with no production of HCl ($v \geq 2$). The degree of vibrational excitation of HCl from secondary abstraction channels is computed to be slightly higher than for the primary channel, which is likely to be a direct consequence of an earlier transition state in the former case.

4.4 HCl angular scattering distributions

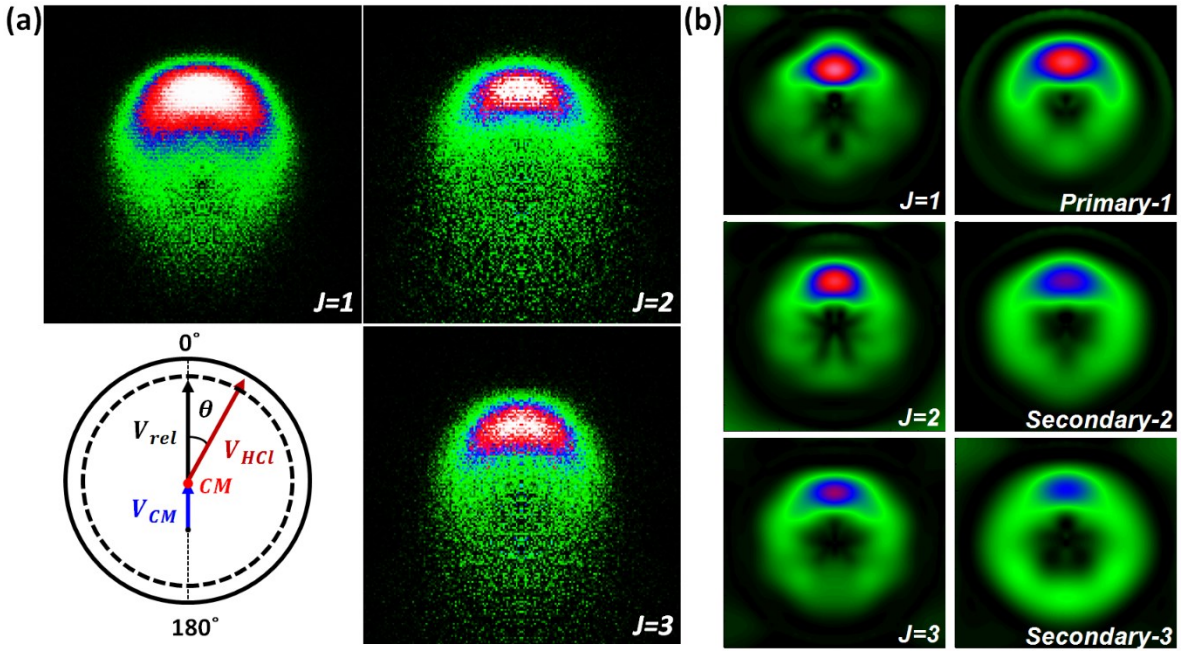

Fig. 5 Representative velocity map images of HCl(v=0, J=1-3) from the Cl + *n*-pentane reaction obtained at an average collision energy of 33.5 kJ mol^{-1}. Velocity map images in panel (a) are recorded from our experiment. The centre of each image locates the velocity of the centre of mass, and the distance from the centre is proportional to the speed in the CM frame. The Newton diagram in the bottom left corner illustrates the directions and magnitudes of the relative velocity vector ($\mathbf{v}_{rel}$), which is parallel to the Cl-atom velocity ($\mathbf{v}_{Cl}$), and the velocity of the centre of mass ($\mathbf{v}_{CM}$). Dashed and solid circles indicate the maximum speeds for HCl(v=0,J=0) following abstraction of a primary or secondary H-atom respectively. Each image is an average of seven separate measurements. Panel (b) shows velocity map images of HCl simulated from the outcomes of the QCT calculations at the same collision energy. The left column contains the simulated images for HCl (v=0, J=1-3), and the right column shows images of HCl (v=0, J=all) products from three different reaction channels. The simulated images are plotted on a different radial scale from the experimental images.

Velocity map images for HCl (v=0, J=1-3) products of reaction (1) are shown in Fig. 5. The images are each averages of seven separate experimental measurements and are symmetrized about the relative

velocity vector (shown in the inset Newton diagram). In principle, because of the experimental method, they require no further correction to extract angular scattering distributions in the CM frame. The differential cross-sections, $d\sigma/d\Omega$ with $d\Omega = dcos\theta d\phi$, extracted from the experimentally obtained images for the J=1 and 3 products by integration over the full range of the radial (speed) coordinate are compared in Fig. 6(a) and show marginally greater sideways or backscattered products at higher J. However, the scattering strongly favours the forward hemisphere and peaks at a scattering angle of 0^o (defined to be parallel to the relative velocity of the reacting Cl atom). The angular distribution is slightly broader than our measurements for the Cl + ethane reaction.

We have previously argued that our method for determining angular scattering distributions might under-represent the contribution from backward scattering because the HCl products that are backward scattered have lower speeds in the laboratory frame.[23,66] These slower products are more prone to secondary collisions with constituents of the *n*-pentane/Ar molecular beam, which can scatter them away from the probe laser. In our usual experimental configuration, the probe laser focus is located either centrally, or slightly above the centre of the *n*-pentane/Ar molecular beam. We tested any possible source of bias from this arrangement by moving the probe laser focus down by 2-mm to favour detection of backward scattered products. We see only a modest enhancement of signal in the backward hemisphere, as shown in the Electronic Supplementary Information, and the error bars in Fig. 6(a) incorporate our best estimate of under-detection at large scattering angles. However, our angular scattering distributions still contain a smaller component of backward scattering than those reported by Suits and coworkers at similar collision energies.[19] These previous experiments were performed using a crossed-molecular beam (CMB) apparatus coupled with VMI and involved ionization of the radical product rather than the HCl. The CMB images are contaminated by background signals associated with the alkane molecular beam that can mask the strongly forward scattered components of the differential cross section. Differences in our angular distributions and those of Suits and coworkers may, therefore, stem from the fact that we probe different products of the reaction, and therefore average differently over the unobserved co-product, or instead derive

from the under-detection of backward scattered products in our experiments, and of forward scattered products in the CMB-VMI studies. The angular distributions that we report are strikingly similar to those obtained in the CMB measurements for faster recoiling products of the Cl + isopentane reaction with kinetic energy release greater than 20 kJ mol^{-1},[19] but the CMB-VMI experiments also report a slower moving contribution that is isotropically scattered, and which we do not observe.

The QCT-computed angular scattering distributions of HCl (v=0, J=1) products from the Cl + *n*-pentane reaction, averaged over all product speeds, are shown in Fig. 6(b). The HCl (v=0) is predominantly forward scattered for all three final rotational levels, and is in quantitative agreement (within experimental uncertainties) with the corresponding DCS extracted from our velocity map images, which is included in Fig. 6(b). This agreement suggests at most a modest degree of undercounting of the back-scattered products in the current measurements. The QCT calculations also predicted DCSs for J>3 products, for which the branching ratios are too low to be observed in the experiments. These calculated DCSs shift systematically to larger scattering angles as J increases, as shown in Fig. 7(a), consistent with our experimental outcomes and prior reports for Cl + alkane reactive scattering.[21,43,44]

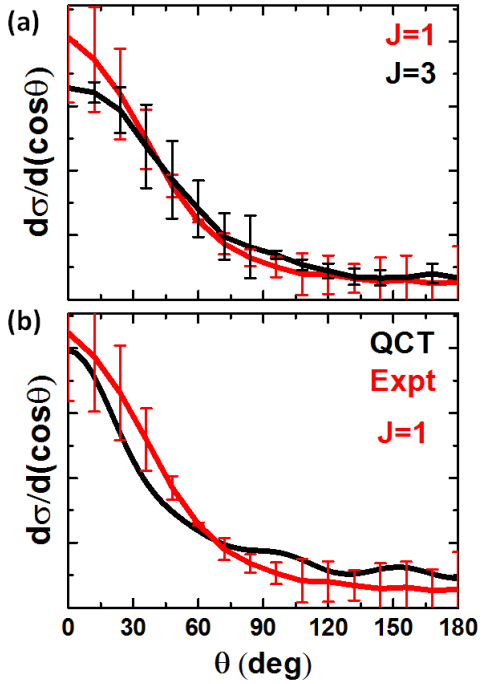

Fig. 6 Angular scattering distributions for HCl (v=0, J=1 and 3) from the Cl + *n*-pentane reaction obtained from the images of Fig. 5 (panel (a)). Computed (black) and experimental (red) angular scattering distributions for HCl (v=0, J=1) are compared in panel (b). All the distributions are normalized to sum to unity.

The quasi-classical trajectories can be sorted by product channel so that we can compare the differences in the reaction dynamics for the three competing abstraction pathways. The computed DCSs for HCl(v=0) products from the three channels are presented in Fig. 7(b). The HCl is mostly forward scattered irrespective of abstraction from a primary or secondary site. However, reaction at a terminal carbon atom most strongly favours forward scattered products, while abstraction from the central carbon atom gives a greater backward scattering fraction. These central H atoms are accessible during collisions at low impact parameter (defined with respect to the centre of the *n*-pentane molecule), which favour rebound dynamics.

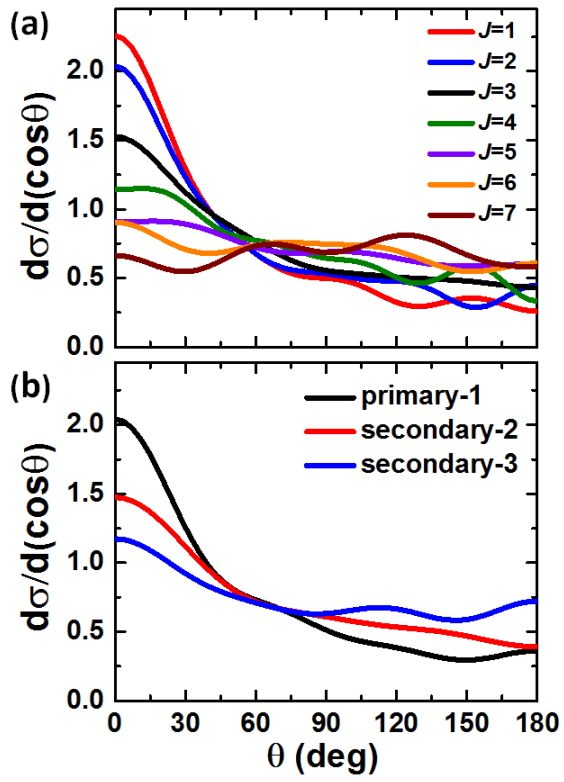

Fig. 7 Differential cross sections for the Cl + *n*-pentane reactions from QCT calculations. (a) Comparisons for HCl (v=0, J) products with J = 1 – 7. (b) HCl (v=0) products, summed over all final J levels, from the three possible reaction channels. All the distributions are normalized to sum to unity.

The pronounced forward scattering peak for HCl products of reaction (1) is a signature of direct stripping dynamics that occur for collisions at large impact parameters. Any backward scattering can be attributed to lower impact parameter collisions. From previous analysis of angular scattering distributions, Rose *et al*. estimated an impact-parameter (b) dependence of the reaction probability (the opacity function, P(b)) for the Cl + neopentane reaction that is essentially constant up to the maximum possible reactive impact parameter b_{max}.[23] This analysis used a model deduced from QCT simulations in which the scattering angle and impact parameter are linearly related. Following the same analysis, we obtain the opacity function shown in Fig. 8(a) for reaction with *n*-pentane. The experimentally deduced reaction probability increases steadily with impact parameter up to almost its maximum value, reflecting the absence of any significant energy barriers to reaction and hence no stringent criteria for sufficient collision energy along the line-of-centres to reach the TS. The computed P(b) vs b plots, presented in Fig. 8(b), are qualitatively similar to that estimated from the experimental DCS data using the model of ref. 23. The maximum impact parameter values are 4.2 Å, 4.6 Å and 5.4 Å for secondary-3, secondary-2 and primary-1 pathways respectively, and the distributions peak at 2.4 Å, 2.7 Å and 3.7 Å. Collisions between Cl atoms and *n*-pentane molecules become less reactive at smaller impact parameters. Instead, larger impact parameter collisions are favoured in which HCl products mostly scatter in the forward direction following a glancing blow between a Cl atom and an *n*-pentane molecule.

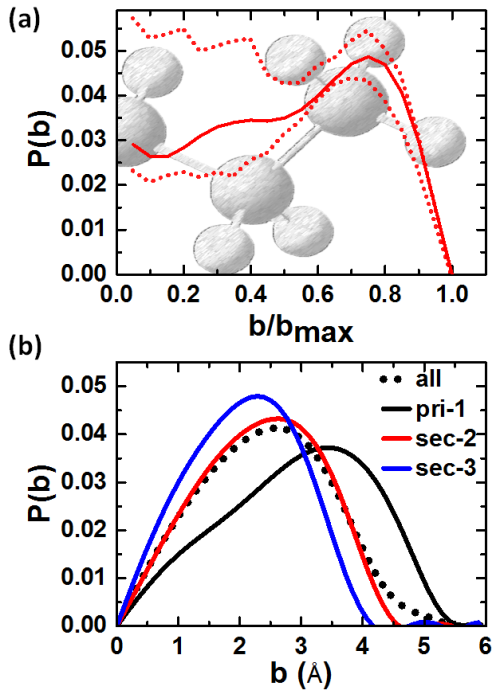

Fig. 8 Opacity functions, P(*b*), for the Cl + *n*-pentane reaction: (a) P(*b*) estimated from analysis of the experimental HCl differential cross sections from Fig. 6 using a model described in ref. 23. The dotted lines capture the uncertainties from this analysis. The plot is superimposed on a qualitative representation of part of the *n*-pentane molecular structure. (b) Computed P(*b*) distributions from QCT calculations for three different H-abstraction reaction pathways (solid lines) and for the outcome from all reactive trajectories (dotted black line). All the distributions are normalized to sum to unity.

4.5 Product kinetic energy release distributions

Analysis of the radial dependence of the experimental velocity images shown in Fig. 5 gives the kinetic energy release of the HCl products, and through conservation of momentum arguments, the total kinetic energy release distributions for the two reaction products. These TKER distributions are plotted in Fig. 9 for products scattered into forward ($0^o \leq \theta \leq 60^o$), sideways ($60^o \leq \theta \leq 120^o$) and backward ($120^o \leq \theta \leq 180^o$) regions. We also compare the TKER distributions obtained by probing HCl(v=0, J=1,2 and 3) products with that derived from measurements of HCl(v=0, J=1) from the Cl + ethane reaction. The TKER limits for abstraction of a primary or a secondary H atom from *n*-pentane are indicated on the plots, and incorporate the effects of the estimated distribution of collision energies. Table 3 lists the average TKERs, expressed as a fraction of the mean collision energy (E_c) for

ease of comparison with the results of Estillore *et al*.[19] whose CMB-VMI experiments were conducted at E_c = 35.1 kJ mol^{-1}.

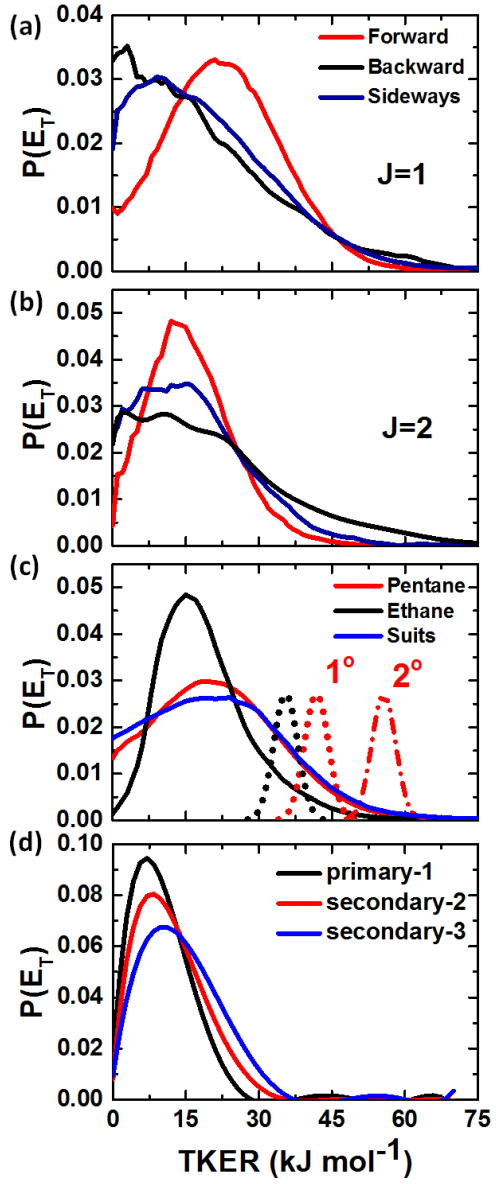

Fig. 9 TKER distributions of both products obtained from velocity map images and QCT calculations of the HCl from Cl + alkane reactions. The upper two panels show scattering-angle dependent TKER distributions for reaction of Cl atoms with *n*-pentane at an average collision energy of 33.5 kJ mol^{-1} derived from images obtained for (a) HCl(v=0,J=1) and (b) HCl(v=0, J=2). In both panels, the red line is for forward (θ = 0˚ - 60˚) scattered HCl, blue is for sideways (60˚ - 120˚) and black for backward (120˚ - 180˚) scattering. All distributions have been scaled to a maximum value of unity. Panel (c) compares the TKER distribution for detection of HCl (v=0, J=1) products from the reaction of Cl + *n*-pentane (red line) with that for the reaction of Cl + ethane (black line) and that deduced by Suits and co-workers for the reaction of Cl + *n*-pentane (blue line) [ref.19] from images of the pentyl radical products obtained at a collision energy of 35.3 kJ mol^{-1}. The dotted black line shows the thermodynamic limit for TKER of the products of the Cl + ethane reaction, with the Gaussian representing the effects of the distribution of collision energies in our experiment. The dotted

and dotted-dashed red curves show the corresponding limits for 1-pentyl and 2- or 3-pentyl radical pathways from the Cl + *n*-pentane reaction in our experiments. Panel (d) shows QCT-computed TKER distributions of the HCl and pentyl radical products of the Cl + *n*-pentane reaction at a collision of 33.5 kJ mol^{-1}. Black is for the primary-1 channel, red is for the secondary-2 channel and blue is for the secondary-3 channel. All the distributions are normalized to sum to unity.

Table 3 Ratios of the mean product total kinetic energy release, ⟨TKER⟩, to the mean collision energy, E_c, for HCl(v=0, J) products of reaction (1). The results are compared with the measurements of Estillore *et al*. [19] in the final column.

	⟨TKER⟩ / E_c			⟨TKER⟩ / E_c
Scattering angle range	HCl(v=0,J=1)	HCl(v=0,J=2)	HCl(v=0,J=3)	From Ref. 19, averaged over HCl(J)
0 – 180^o	0.66	0.62	0.51	0.63
Forward	0.70	0.63	0.50	0.66
Sideways	0.61	0.61	0.52	0.57
Backward	0.58	0.66	0.63	0.67

An average of our ⟨TKER⟩ / E_c ratios for HCl(v=0, J=1−3) weighted by our measured distribution of rotational level populations gives ⟨⟨TKER⟩/E_c⟩ = 0.60 (for all scattering angles). The TKER distributions are very similar to those reported by Estillore *et al*. from measurements of the velocities of the radical co-products at a similar mean collision energy (see Fig. 9(c) and Table 3).

Several trends are evident from the plots in Fig. 9. In each panel, the majority of the TKER distribution lies within the thermodynamic limit for abstraction of a primary H-atom, but a tail extends to the limit expected for secondary H-atom abstraction. The TKER distribution is shifted upwards in energy for the Cl + *n*-pentane reaction when compared to our measured distribution for Cl + ethane, but both peak at the same value of TKER / E_c = 0.72. The experimental data in isolation point to both mechanisms (1a) and (1b) being active, consistent with the room-temperature studies of Cl + propane

and Cl + *n*-butane reactions by Tyndall *et al*.[36] and the CMB experiments for Cl + $CD_3CH_2CH_2CD_3$ by Estillore *et al*.[39] However, the relative contributions cannot be extracted from our experimental measurements and are better estimated from our QCT calculations (see Section 4.6).

The product TKER is larger for a reaction producing HCl(v=0, J=1) than for HCl(v=0, J=2), and the TKER is further reduced for the channel leading to HCl(v=0, J=3). The differences cannot be accounted for by the changes in rotational energy of the HCl, and therefore imply that additional rotational or vibrational excitation of the pentyl radical co-product accompanies greater HCl rotational excitation. The mean values of the TKER distributions for forward, sideways and backward scattered HCl(v=0, J=1) products are, respectively, 23.5 kJ mol^{-1}, 20.5 kJ mol^{-1} and 19.5 kJ mol^{-1}. This trend is consistent with larger impact parameters that conserve a substantial fraction of the collision energy into product TKER causing the forward scatter, whereas low-*b* collisions and backward scatter allow greater coupling of the initial collision energy into internal degrees of freedom of the radical product. This argument is further supported by the scattering distributions of Fig. 6(a) and Fig. 7(a), which show an enhancement of back scattered products as J increases.

Computed TKER distributions for the three competing reaction channels are shown in Fig. 9 (d), and are narrower than the experimental measurements. H abstraction from the central carbon atom gives the fastest products, whereas the TKER distribution for the primary-1 pathway peaks at a similar energy to that for the secondary-2 channel. However, the TKER distributions for the secondary abstraction channels are broader. The averages of the QCT-calculated TKER distributions for primary-1, secondary-2 and secondary-3 abstraction channels are 9.7 kJ mol^{-1}, 11.8 kJ mol^{-1} and 14.0 kJ mol^{-1} respectively, which are all lower than the experimental observations. After accounting for the kinetic energy release to the products, the balance of the available energy from the reaction must be taken up by vibrational and rotational degrees of freedom of the pentyl radical. The discrepancy between experiment and simulation may therefore be a consequence of a classical treatment of the internal motions of the pentyl radical in the QCT calculations.

4.6 Branching between primary and secondary abstraction channels

The relative importance of the primary and secondary H-atom abstraction channels at our super-thermal collision energies cannot be distinguished from our velocity map imaging measurements. However, the QCT calculations allow us to extract the branching ratios. The simulations show the relative reaction cross-sections *per hydrogen atom* for the three reaction channels are 1.0 : 3.5 : 3.0 for reaction at a primary C1-H (or C5-H) site, a secondary C2-H or C4-H site and a secondary C3-H site. Hence, one quarter of the total HCl products of Cl + *n*-pentane reaction derive from the primary H-atom abstraction channel, whereas a purely statistical ratio would predict one half of reactions to occur at a primary site. The earlier TS for secondary H-atom abstraction biases the reaction towards these pathways. The site-propensity emerging from our QCT calculations is similar to the observations by Tyndall *et al*. of primary vs secondary abstraction branching ratios in reactions of Cl atoms with propane and *n*-butane.[36]

4.7 Dynamical stereochemistry

The likelihood of a chemical reaction occurring is influenced not only by the energies and locations of transition states along the reaction path, but also by steric constraints on the geometry for reaction. A simple but convenient way to describe the steric requirements of a chemical reaction is the cone-of-acceptance model,[65] but the textbook version of this model is inadequate in the case of a reaction with no true barrier. However, the geometrical requirements can be explored for Cl + alkane reactions on the basis of our QCT calculations on a PES that has been successfully tested against experimental REMPI and VMI data. Fig. 10 shows reaction cross sections plotted as a function of two internal coordinates, the polar ψ and azimuthal ϕ angles of approach of the Cl atom with respect to the reactive C-H bond axis. The method of generation of these plots is described in the Electronic Supplementary Information. The outcomes from reactive trajectories propagated on the full PES for

individual primary and secondary H atom abstraction are presented and compared in the bottom row of Fig. 10.

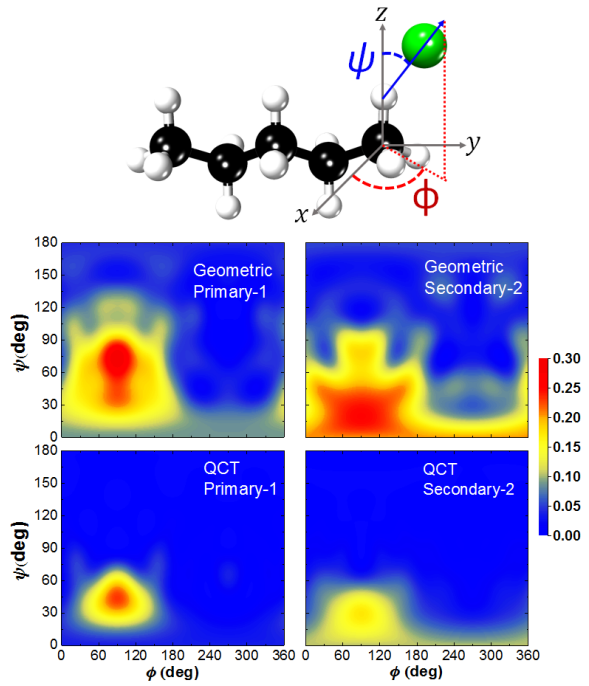

Fig. 10 Preferential geometries of approach of a Cl atom to the reactive C-H bond axis in the entrance channel of the PES. The reaction probabilities of primary (column 1) and secondary (column 2) abstraction channels are compared as a function of two internal angles ψ and ϕ defined relative to the reactive C-H bond, as is illustrated for the primary channel at the top of the figure. The upper row shows the results from a geometrical model, and the lower row shows the outcomes of the reactive trajectories on the full PES.

To ascertain the influence of purely geometric effects on the preferred angles of attack of Cl atoms at primary and secondary H atoms in *n*-pentane, a simpler model was also invoked. A batch of 50,000 trajectories was run in which all intra and intermolecular interactions were set to zero. In this geometric model, a trajectory was terminated if the distance between the Cl atom and any atom of the *n*-pentane molecule decreased to 1.5 Å. Those trajectories where the distance between the Cl atom and any H atom reached 1.5 Å were marked as reactive. The outcomes are shown in the top row of Fig. 10 for attack at primary and secondary H-atoms.

The various plots in Fig. 10 show that secondary abstraction is favoured for close to collinear (ψ = 0°) geometry of the TS, but that the angle of approach can be up to 60° for successful trajectories. This range of attack angles is consistent with the scattering angle distribution of HCl products. However, primary abstraction is favoured for ψ values of ~45°, and a ~30° range of angles. This deviation from collinear approach for primary abstraction might account for the production of slightly rotationally hotter HCl products than from secondary abstraction pathways.

Further analysis of the dynamical stereochemistry revealed by the QCT calculations shows that the PES is most attractive at a geometry where the chlorine atom can interact simultaneously with multiple H atoms (a C1-H and a C3-H, or a C2-H and a C4-H, or three C1-H together) instead of collinear approach to individual H atoms in the entrance channel. This propensity is illustrated schematically in the inset image in Fig.1. These localised attractive regions of the PES encourage the C-H-Cl angle to deviate from the preferred collinearity in the TS, and reduce the reaction probability at low impact parameter. Hence, the detailed nature of the PES on the reactants' side can be linked to the preferred forward scattering of HCl products from the Cl + *n*-pentane reaction.

5. Conclusions

Comparisons have been drawn between experimental and computational studies of the Cl + *n*-pentane reaction at a collision energy of 33.5 $\pm$ 8.4 kJ mol^{-1}. The experimental measurements used REMPI spectroscopy and velocity map imaging of nascent products to deduce rotational level population distributions and quantum-state resolved differential cross sections. These detailed experimental outcomes are satisfactorily reproduced by quasi-classical trajectories propagated on a global potential energy surface obtained by empirical valence bond fits to *ab initio* electronic structure calculations. The reasonable results obtained from this new PES permit new dynamical insights to be

drawn from the QCT calculations beyond what can be deduced from analysis of the experimental data alone.

At our chosen collision energy, the Cl + *n*-pentane reaction produces HCl by both primary and secondary H-atom abstraction channels. Competition between three different reactions corresponding to removal of hydrogen atoms bonded to the C1 and C5, C2 and C4, and C3 carbon atoms gives a branching ratio of 1.0 : 3.5 : 3.0 per H-atom site. The earlier TS for secondary rather than primary H-atom abstraction enhances reaction at the C2, C3 and C4 sites compared to purely statistical expectations. The rotational temperature of the HCl is 138 ± 13 K, which is similar to the outcomes of Cl + ethane and Cl + neopentane reactions for which there is only a primary H-atom abstraction pathway. The QCT calculations indicate that both primary and secondary H-atom abstractions produce rotationally cold HCl. Any post-transition-state dynamics that affect the degree of rotational excitation of the HCl are therefore governed by similar interactions for reaction at primary and secondary sites, notwithstanding the greater energy release associated with the secondary radical formation pathway. We see no evidence for the formation of vibrationally excited HCl in the experiments, and modest (<10%) branching to HCl(v=1) in the QCT calculations. The HCl scattering peaks strongly in the forward direction in both experimental and computational studies, but covers a broad angular range, consistent with a wide range of impact parameters for this barrierless reaction. Using a model previously applied to the Cl + neopentane reaction, we estimate approximately constant reactivity at all impact parameters up to the maximum value, with a weak preference for reaction at the periphery. This analysis is borne out by QCT calculations of the opacity function.

The total kinetic energy release distributions for the HCl and pentyl radical products agree well with a previous report in which the pentyl radical was detected. The kinetic energy release is greater for forward than for sideways and backward scattered products. It decreases as the rotational quantum number of the HCl increases, indicating that greater rotational excitation of the HCl is accompanied

by higher internal energy in the pentyl radical co-product. The QCT calculations underestimate the TKER of the reaction products; hence, on energy balance grounds, the calculations overestimate the internal energy of the pentyl radicals. The classical treatment of the vibrational modes of the pentyl products may be responsible for this discrepancy.

The EVB PES reported here is the first global PES for Cl-atom reaction with an alkane larger than methane[24] and ethane.[27] Critical comparisons with experimental measurements, albeit at a superthermal collision energy, suggest that the new PES is sufficiently accurate to describe well the reactive scattering dynamics of Cl atoms with pentane as a representative higher alkane molecule.

Acknowledgements

This work is funded by EPSRC Programme Grant EP/L005913/1. GTD thanks the EPSRC for a Doctoral Training Grant studentship and SP gratefully acknowledges the University of Bristol for the award of a postgraduate scholarship. We thank Prof J.N. Harvey and Dr D.P. Tew for helpful discussions about the electronic structure calculations.

References

1 C. W. Spicer, E. G. Chapman, B. J. Finlayson-Pitts, R. A. Plastridge, J. M. Hubbe, J. D. Fast and C. M. Berkowitz, *Nature*, 1998, **394**, 353–356.

2 C. J. Young, R. A. Washenfelder, P. M. Edwards, D. D. Parrish, J. B. Gilman, W. C. Kuster, L. H. Mielke, H. D. Osthoff, C. Tsai, O. Pikelnaya, J. Stutz, P. R. Veres, J. M. Roberts, S. Griffith, S. Dusanter, P. S. Stevens, J. Flynn, N. Grossberg, B. Lefer, J. S. Holloway, J. Peischl, T. B. Ryerson, E. L. Atlas, D. R. Blake and S. S. Brown, *Atmos. Chem. Phys.*, 2014, **14**, 3427–3440.

3 J. D. DeSain, S. J. Klippenstein and C. A. Taatjes, *Phys. Chem. Chem. Phys.*, 2003, **5**, 1584–1592.

4 C. A. Taatjes, *J. Phys. Chem. A*, 2006, **110**, 4299–312.

5 D. D. Riemer, E. C. Apel, J. J. Orlando, G. S. Tyndall, W. H. Brune, E. J. Williams, W. A. Lonneman and J. D. Neece, *J. Atmos. Chem.*, 2008, **61**, 227–242.

6 I. Suh and R. Zhang, *J. Phys. Chem. A*, 2000, **104**, 6590–6596.

7 A. D. Estillore, L. M. Visger and A. G. Suits, *J. Chem. Phys.*, 2010, **133**, 074306.

8 T. J. Preston, G. T. Dunning, A. J. Orr-Ewing and S. A. Vázquez, *J. Phys. Chem. A*, 2014, **118**, 5595–5607.

9 B. Joalland, Y. Shi, A. Kamasah, A. G. Suits and A. M. Mebel, *Nat Commun*, 2014, **5**, 4064.

10 B. Hornung, T. J. Preston, S. Pandit, J. N. Harvey and A. J. Orr-Ewing, *J. Phys. Chem. A*, 2015, **119**, 9452–9464.

11 C. Murray and A. J. Orr-Ewing, *Int. Rev. Phys. Chem.*, 2004, **23**, 435–482.

12 C. Murray, J. K. Pearce, S. Rudić, B. Retail and A. J. Orr-Ewing, *J. Phys. Chem. A*, 2005, **109**, 11093–11102.

13 B. Joalland, Y. Shi, A. D. Estillore, A. Kamasah, A. M. Mebel and A. G. Suits, *J. Phys. Chem. A*, 2014, **118**, 9281–9295.

14 J. Park, Y. Lee, J. F. Hershberger, J. M. Hossenlopp and G. W. Flynn, *J. Am. Chem. Soc.*, 1992, **114**, 58–63.

15 W. R. Simpson, T. P. Rakitzis, S. A. Kandel, A. J. Orr-Ewing and R. N. Zare, *J. Chem. Phys.*, 1995, **103**, 7313.

16 S. Yoon, S. Henton, A. N. Zivkovic and F. F. Crim, *J. Chem. Phys.*, 2002, **116**, 10744.

17 B. Zhang and K. Liu, *J. Chem. Phys.*, 2005, **122**, 101102.

18 D. A. Blank, N. Hemmi, A. G. Suits and Y. T. Lee, *Chem. Phys.*, 1998, **231**, 261–278.

19 A. D. Estillore, L. M. Visger and A. G. Suits, *J. Chem. Phys.*, 2010, **132**, 164313.

20 M. J. Bass, M. Brouard, C. Vallance, T. N. Kitsopoulos, P. C. Samartzis and R. L. Toomes, *J. Chem. Phys.*, 2004, **121**, 7175–7186.

21 R. L. Toomes and T. N. Kitsopoulos, *Phys. Chem. Chem. Phys.*, 2003, **5**, 2481–2483.

22 R. L. Toomes, A. J. van den Brom, T. N. Kitsopoulos, C. Murray and A. J. Orr-Ewing, *J. Phys. Chem. A*, 2004, **108**, 7909–7914.

23 R. A. Rose, S. J. Greaves and A. J. Orr-Ewing, *J. Chem. Phys.*, 2010, **132**, 244312.

24 B. Hornung, J. N. Harvey, T. J. Preston, G. T. Dunning and A. J. Orr-Ewing, *J. Phys. Chem. A*, 2015, **119**, 9590–9598.

25 S. Rudić, C. Murray, J. N. Harvey and A. J. Orr-Ewing, *J. Chem. Phys.*, 2004, **120**, 186–198.

26 S. J. Greaves, J. Kim, A. J. Orr-Ewing and D. Troya, *Chem. Phys. Lett.*, 2007, **441**, 171–175.

27 S. J. Greaves, A. J. Orr-Ewing and D. Troya, *J. Phys. Chem. A*, 2008, **112**, 9387–95.

28 G. Czakó and J. M. Bowman, *Science*, 2011, **334**, 343–346.

29 S. Rudić, C. Murray, D. Ascenzi, H. Anderson, J. N. Harvey and A. J. Orr-Ewing, *J. Chem. Phys.*, 2002, **117**, 5692.

30 S. Rudic, C. Murray, J. N. Harvey and A. J. Orr-Ewing, *Phys. Chem. Chem. Phys.*, 2003, **5**, 1205–1212.

31 C. Murray, B. Retail and A. J. Orr-Ewing, *Chem. Phys.*, 2004, **301**, 239–249.

32 G. S. Tyndall, J. J. Orlando, T. J. Wallington, M. Dill and E. W. Kaiser, *Int. J. Chem. Kinet.*, 1997, **29**, 43–55.

33 N. Choi, M. J. Pilling, P. W. Seakins and L. Wang, *Phys. Chem. Chem. Phys.*, 2006, **8**, 2172–2178.

34 Y. F. Yen, Z. Wang, B. Xue and B. Koplitz, *J. Phys. Chem.*, 1994, **98**, 4–7.

35 A. J. Orr-Ewing, *Annu. Rev. Phys. Chem.*, 2015, **66**, 119–141.

36 G. S. Tyndall, J. J. Orlando, T. J. Wallington, M. Dill and E. W. Kaiser, *Int. J. Chem. Kinet.*, 1997, **29**, 43–55.

37 D. F. Varley and P. J. Dagdigian, *Chem. Phys. Lett.*, 1996, **255**, 393–400.

38 D. F. Varley and P. J. Dagdigian, *J. Phys. Chem.*, 1996, **100**, 4365–4374.

39 A. D. Estillore, L. M. Visger-Kiefer, T. A. Ghani and A. G. Suits, *Phys. Chem. Chem. Phys.*, 2011, **13**, 8433–8440.

40 B. Joalland, Y. Shi, N. Patel, R. Van Camp and A. G. Suits, *Phys. Chem. Chem. Phys.*, 2014, **16**, 414–420.

41 H.-B. Qian, D. Turton, P. W. Seakins and M. J. Pilling, *Int. J. Chem. Kinet.*, 2002, **34**, 86–94.

42 N. Hemmi and A. G. Suits, *J. Chem. Phys.*, 1998, **109**, 5338.

43 C. Murray and A. J. Orr-Ewing, *Int. Rev. Phys. Chem.*, 2004, **23**, 435–482.

44 M. J. Bass, M. Brouard, C. Vallance, T. N. Kitsopoulos, P. C. Samartzis and R. L. Toomes, *J. Chem. Phys.*, 2003, **119**, 7168.

45 A. Warshel and R. M. Weiss, *J. Am. Chem. Soc.*, 1980, **102**, 6218–6226.

46 A. Warshel, *Acc. Chem. Res.*, 1981, **14**, 284–290.

47 S. J. Greaves, R. A. Rose and A. J. Orr-Ewing, *Phys. Chem. Chem. Phys.*, 2010, **12**, 9129–9143.

48 D. S. Green, G. A. Bickel and S. C. Wallace, *J. Mol. Spectrosc.*, 1991, **150**, 388–469.

49 D. H. Parker and A. T. J. B. Eppink, *J. Chem. Phys.*, 1997, **107**, 2357.

50 T. H. Dunning, *J. Chem. Phys.*, 1989, **90**, 1007.

51 R. A. Kendall, T. H. Dunning and R. J. Harrison, *J. Chem. Phys.*, 1992, **96**, 6796.

52 T. H. Dunning, K. A. Peterson and A. K. Wilson, *J. Chem. Phys.*, 2001, **114**, 9244.

53 P. C. Hariharan and J. A. Pople, *Theor. Chim. Acta*, 1973, **28**, 213–222.

54 M. M. Francl, *J. Chem. Phys.*, 1982, **77**, 3654.

55 M.J. Frisch, G.W. Trucks, H.B. Schlegel, G.E. Scuseria, M.A. Robb, J.R. Cheeseman, G. Scalmani, V. Barone, B. Mennucci, G.A. Petersson, H. Nakatsuji, M. Caricato, X. Li, H.P. Hratchian, A.F. Izmaylov, J. Bloino, G. Zheng, J.L. Sonnenberg, M. Hada, M. Ehara, K. Toyota, R. Fukuda, J. Hasegawa, M. Ishida, T. Nakajima, Y. Honda, O. Kitao, H. Nakai, T. Vreven, J.A. Montgomery Jr., J.E. Peralta, F. Ogliaro, M. Bearpark, J.J. Heyd, E. Brothers, K.N. Kudin, V.N. Staroverov, R. Kobayashi, J. Normand, K. Raghavachari, A. Rendell, J.C. Burant, S.S. Iyengar, J. Tomasi, M. Cossi, N. Rega, J.M. Millam, M. Klene, J.E. Knox, J.B. Cross, V. Bakken, C. Adamo, J. Jaramillo, R. Gomperts, R.E. Stratmann, O. Yazyev, A.J. Austin, R. Cammi, C. Pomelli, J.W. Ochterski, R.L. Martin, K. Morokuma, V.G. Zakrzewski, G.A. Voth, P. Salvador, J.J. Dannenberg, S. Dapprich, A.D. Daniels, Ö. Farkas, J.B. Foresman, J. V Ortiz, J. Cioslowski, and D.J. Fox, GAUSSIAN 09 (Revision E.01), Gaussian Inc., Wallingford CT, 2009.

56 K. E. Yousaf and K. A. Peterson, *J. Chem. Phys.*, 2008, **129**, 184108.

57 K. A. Peterson, T. B. Adler and H.-J. Werner, *J. Chem. Phys.*, 2008, **128**, 084102.

58 T. J. Preston, B. Hornung, S. Pandit, J. N. Harvey and A. J. Orr-Ewing, *J. Phys. Chem. A*, 2016, **120**, 4672–4682.

59 R. B. Bernstein, *Atom-molecule collision theory: a guide for the experimentalist*, Plenum Press, 1979.

60 F. J. Aoiz, L. Banares and V. J. Herrero, *J. Chem. Soc.{,} Faraday Trans.*, 1998, **94**, 2483–2500.

61 F. J. Aoiz, V. J. Herrero and V. Sáez Rábanos, *J. Chem. Phys.*, 1992, **97**, 7423.

62 C. M. Western, *J. Quant. Spectrosc. Radiat. Transf.*, 2016.

63 S. Rudić, D. Ascenzi and A. J. Orr-Ewing, *Chem. Phys. Lett.*, 2000, **332**, 487–495.

64 C. A. Picconatto, A. Srivastava and J. J. Valentini, *J. Chem. Phys.*, 2001, **114**, 1663.

65 R. D. Levine, *Molecular Reaction Dynamics*, Cambridge University Press, Cambridge, 2005.

66 R. A. Rose, S. J. Greaves and A. J. Orr-Ewing, *Mol. Phys.*, 2010, **108**, 981–992.

Graphical Abstract